

A machine learning strategy for modeling and optimal design of near-field radiative heat transfer

Cite as: Appl. Phys. Lett. **121**, 000000 (2022); doi: 10.1063/5.0103363

Submitted: 15 June 2022 · Accepted: 28 July 2022 ·

Published Online: 0 Month 0000



Shizheng Wen, Chunzhuo Dang, and Xianglei Liu^{a)}

AFFILIATIONS

School of Energy and Power Engineering, Nanjing University of Aeronautics and Astronautics, Nanjing 210016, China

Note: This paper is part of the APL Special Collection on Thermal Radiation at the Nanoscale and Applications.

^{a)} Author to whom correspondence should be addressed: xliu@nuaa.edu.cn

ABSTRACT

The recent decade has witnessed the advent of near-field radiative heat transfer (NFRHT) in a wide range of applications, including thermal photovoltaics and thermal diodes. However, the design process for these thermal devices has remained complex, often relying on the intuition and expertise of the designer. To address these challenges, a machine learning (ML) strategy based on the combination of an artificial neural network (ANN) and a genetic algorithm (GA) is presented. The ANN is trained to model representative scenarios, viz., NFRHT between meta-materials and NFRHT and thermal rectification between nanoparticles. The influence of different problem complexities, i.e., the number of input variables of function to be fitted, on effectiveness of the trained ANN is investigated. Test results show that ANNs can obtain the radiative heat flow and rectification ratio accurately and rapidly. Subsequently, physical parameters for the largest radiative heat flow and rectification ratio are determined by the utilization of GA on the trained ANN, and underlying mechanisms of deterministic optimum are discussed. Our work shows that data-driven ML methods are a powerful tool, which offers unprecedented opportunities for future NFRHT research.

Published under an exclusive license by AIP Publishing. <https://doi.org/10.1063/5.0103363>

Near-field radiative heat transfer (NFRHT) has many promising applications in a variety of fields from electronic devices to renewable energy utilization due to its high efficiency of energy transmission.^{1–6} Previous theoretical research mainly focuses on cases of enhancing the radiative heat transfer far beyond the black-body limit (thermal photovoltaics,^{7–11} thermal imaging^{12–14}) and active control of the heat flow (thermal diodes,^{15,16} transistors,¹⁷ and switches^{18–20}). Common methods in previous designs of enhancing and controlling heat flow include inducing surface and hyperbolic modes, employing new materials whose dielectric function is sensitive to the temperature and exploiting asymmetric nanophotonic structures.^{21–26} Nevertheless, these methods very often rely on the intuition and expertise of researchers, ultimately limiting the development of structure for desired radiative properties. Additionally, conventional methods of calculating NFRHT, including rigorous coupled-wave analysis (RWCA)^{1,27,28} and dyadic Green's functions (DGFs),^{29,30} are very computationally expensive. Therefore, exploring a more systematic and efficient method to design thermal devices is very imperative.

In recent years, the advancement of machine learning (ML) algorithms and the abundance of open source software may provide alternative ways for researchers to tackle optimization problems in

near-field radiative heat transfer. Prompted by ML's attractive advantages, such as identifying multi-dimensional correlations and exploring massive design spaces, thermal-science research has successfully begun to employ ML, thereby bringing fresh perspectives to its conventional problems.^{31–34} In the field of thermal radiation, a large body of researchers are developing ML assisted code that can be efficiently used to optimize structures for a specific purpose.^{35,36} For example, Ben-Abdallah *et al.*^{37,38} designed the composite structures to control the thermal emission and local density of state based on genetic algorithms (GAs). Hu *et al.*³⁹ took the power density and system efficiency as the coupling parameters to optimize the Tamm emitter based on the Monte Carlo tree search algorithm. Sakurai *et al.*⁴⁰ designed an ultranarrow-band wavelength-selective thermal radiator by combining the electromagnetic field calculation and Bayesian optimization. Seo *et al.*⁴¹ applied an evolutionary algorithm to find the optimal geometric parameters of a solar thermal absorber for the largest solar absorptance. However, recent progress on this topic has mainly focused on harnessing solar radiation for power generation, and the characteristic scale of it is in the far-field radiative heat transfer. The more modern and hotter topics about how ML can be effectively applied in NFRHT remain unclear.

In this work, by combining two data-driven ML methods, viz., artificial neural networks (ANNs)⁴² and genetic algorithms (GAs), we propose a flow chart for modeling and optimal design of near-field thermal devices as shown in Fig. 1. The adopted workflow is enabled by the following innovative points: first, a sampling method based on Latin hypercube sampling (LHS) and sensitivity analysis (SA) is used for the design parameters of the problem to be studied. These sampled points are calculated with an accurate NFRHT method so as to build our training datasets. Second, a surrogate ANN model was trained to construct a functional model from an input feature vector to a corresponding output feature vector, which can be used to predict the NFRHT and rectification ratio of corresponding structures. Finally, GA was applied to the surrogate ANN model to identify the optimal solution for the problem based on emulating biological evolutionary theories.^{43,44} Detailed descriptions and settings of ANN and GA for this research can be seen in the [supplementary material](#).

To illustrate these ideas, the proposed workflow has been first dedicated to tackling the structural optimization of NFRHT between multilayered metamaterials, which shows unprecedented potentials to manipulate light and heat beyond substances existing in nature. NFRHT between two periodic multilayered metamaterials configured

by doped silicon (D-Si) and germanium (Ge) in Ref. 45 are reconsidered. The system under consideration is shown in Fig. 2. In the modeling, t_m and t_d are the thicknesses of D-Si (metallic behavior) and Ge (dielectric), respectively. The resulting period $P = t_m + t_d$ is set to 50 so as to approximate a semi-infinite structure. Metal-dielectric (MD) configuration for the two layers adjacent to vacuum is employed. The temperature of each body is assumed to be uniform at T_h and T_l . The dielectric function of D-Si (n-type) with a doping concentration of D_{si} is obtained from Ref. 46. The relative permittivity of vacuum and Ge is treated as constants 1 and 16, respectively. NFRHT between two multilayered structures can be described as

$$Q_{pla} = \frac{1}{4\pi^2} \int_0^\infty [\Theta(\omega, T_1) - \Theta(\omega, T_2)] d\omega \times \int_0^\infty \beta \sum_{j=s,p} \xi_j(\omega, \beta) d\beta, \quad (1)$$

where $\Theta(\omega, T)$ represents the mean energy of Planck's oscillator, $\xi_j(\omega, \beta)$ is the energy transmission coefficient depending on the reflection coefficient matrix of the structure, and j is either s or p for different polarizations. In the present study, the scattering theory and

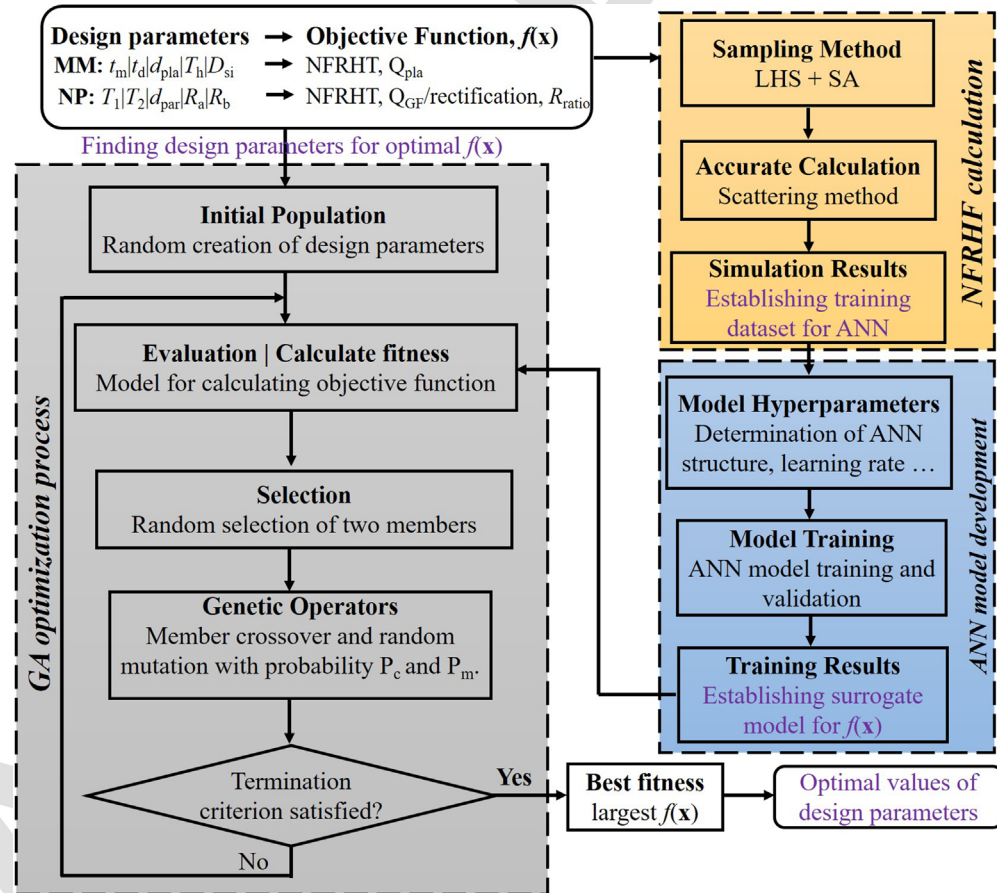


FIG. 1. Outline of the proposed machine learning strategy. Goal of this workflow is to model the NFRHT/rectification ratio (objective function) between multilayered metamaterials (MMs) and nanoparticles (NPs) and decide design parameters for the largest value of objective functions.

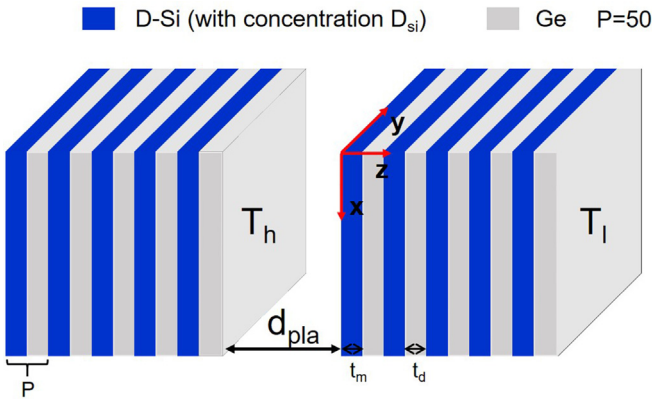


FIG. 2. Schematic of near-field thermal radiation between two multilayered meta-materials (at temperatures T_h and T_l , respectively), separated by a vacuum gap d_{pla} . The thickness of D-Si with a doping concentration of D_{si} and Ge layers are t_m and t_d , respectively, resulting in a unit cell of period $P = t_m + t_d$.

effective medium theory (EMT) in Ref. 45 are used to calculate the accurate and approximate value of energy transmission coefficient, respectively.

Usually, when the functional relationship between input α and output Q_{ANN} becomes more complex, larger training dataset and network architectures are required so as to retain good prediction performance.⁴⁷ To better reflect the applicability of ANNs to problems with different complexities, four different functional models were considered, including two-input model {input: (t_m , t_d), output: Q_{pla} }, three-input model {input: (t_m , t_d , d_{pla}), output: Q_{pla} }, four-input model {input: (t_m , t_d , d_{pla} , T_h), output: Q_{pla} }, and five-input model {input: (t_m , t_d , d_{pla} , T_h , D_{si}), output: Q_{pla} }. The range of considered variables for sampling is shown in Table I. Parameters will take the default value if they are not considered as input variables. The temperature of T_l is taken as 0 K in all cases.

A uniformly distributed sampling method like LHS is first used, and four different sizes of training datasets without prejudice (1000, 2000, 3000, and 4000) are obtained toward problems with different complexities. However, according to Refs. 48 and 49, neural networks are biased toward learning less complex functions, and uniform input data distributions over the parameter space struggle to learn high-gradient components and often fail to train. To address this challenge, non-uniform input data distributions are generated, and more sampled points in high-gradient regions are conducted additionally sampling. We mainly implement the global sensitivity analysis (GSA) to help us identify the essential parameters for the steep variation

TABLE I. Range of considered variables for multilayer metamaterials.

Parameter ^a	t_m	t_d	d_{pla}	T_h	D_{si}
Lower bound	10	10	10	300	1×10^{18}
Upper bound	500	500	500	400	1×10^{20}
Default value			100	300	1×10^{20}

^aUnits for t_m , t_d , and d_{pla} are nanometer (nm). Units for T_h and D_{si} are Kelvin (K) and cm^{-3} , respectively.

TABLE II. Adjusted- R^2 results for the ANN model of four different inputs.

Category	Two-input	Three-input	Four-input	Five-input
Adjusted- R^2	1	1	0.9998	0.9996

(gradients), thereby generating our additionally sampled points. The results show that the vacuum gap distance d_{pla} is the most influential parameter, aligning with the existing evanescent wave theory in NFRHT. Additional 300 points, 400 points, and 500 points for three-input, four-input, and five-input models, were sampled in regions with small values of d_{pla} . Subsequently, these training datasets and four different ANN architectures are applied to train the model. More details about sampling methods and training process can see the [supplementary material](#).

Adjusted coefficients of determination (Adjusted- R^2) are used to characterize the performance of the developed model, which can be expressed as follows:

$$R^2 = 1 - \frac{\sum_{i=1}^n (y_{\text{predict},i} - y_{\text{data},i})^2}{\sum_{i=1}^n (y_{\text{data},i} - \bar{y}_{\text{data},i})^2}, \quad (2a)$$

$$\text{Adjusted} - R^2 = 1 - \frac{(1 - R^2)(n - 1)}{n - k - 1}, \quad (2b)$$

where $y_{\text{predict},i}$ is the value predicted by ANNs at test data point i , $y_{\text{data},i}$ is the actual value calculated by the scatter theory at point i , n is the size of the test dataset, and k is the number of input variables for the model. The results of trained models on test dataset (100 points generated by LHS) are shown in Table II. It can be clearly seen that Adjusted- R^2 for four models is approximately 1. This suggests that prediction results of the neural network are in good agreement with true values in considered ranges. In Fig. 3, we show errors of different testing structures predicted by the five-input ANN and EMT. The error is defined by the following equation:

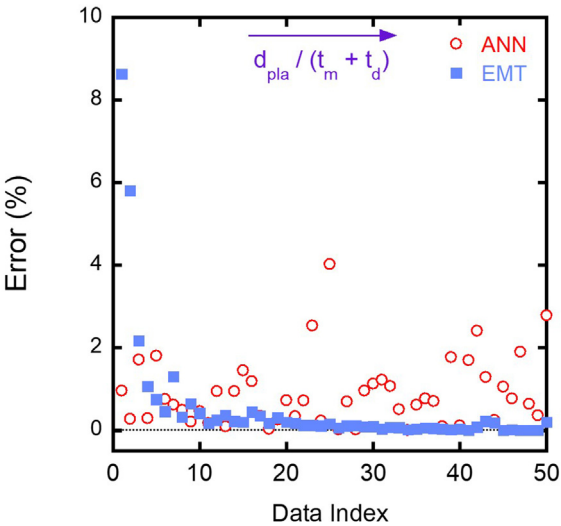


FIG. 3. The errors of different testing structures predicted by ANN and EMT. The testing data sets are randomly generated by LHS. In order to shown the characteristics of EMT, we sort the data by $d_{pla} / (t_m + t_d)$.

TABLE III. Optimization results for the ANN surrogate model of four different inputs. Numbers in brackets indicate the default value of corresponding parameters. Q_{ANN} is the radiative heat flow predicted by the ANN. Q_{scatter} is the accurate heat flow calculated by the scatter theory on the deterministic optimum. Error is defined in Eq. (3).

Category ^a	t_m	t_d	d_{pla}	T_h	D_{si}	Q_{ANN}	Q_{scatter}	Error
Two-input	10	10	(100)	(300)	(1×10^{20})	6744	6438	4.75%
Three-input	10	10	10	(300)	(1×10^{20})	191883	197550	2.87%
Four-input	320	10	10	400	(1×10^{20})	666398	623320	6.91%
Five-input	500	10	10	400	1.93×10^{19}	1334861	1391800	4.09%

^aUnits for Q_{ANN} and Q_{scatter} are W/m^2 .

$$\text{Error} = \left| \frac{Q_{\text{predicted}} - Q_{\text{accurate}}}{Q_{\text{accurate}}} \right|. \quad (3)$$

the application conditions of EMT in NFRHT between multilayer metamaterials.⁴⁵ In contrast, the ANN model can have relative small errors (less than 5%) in all ranges.

Subsequently, the trained ANN is used as a surrogate model, and another ML technique, viz., genetic algorithm, is applied for finding

From the results, we can see that only when $d_{\text{pla}}/(t_m + t_d)$ is large enough, can EMT be accurate to predict the NFRHT. This aligns with

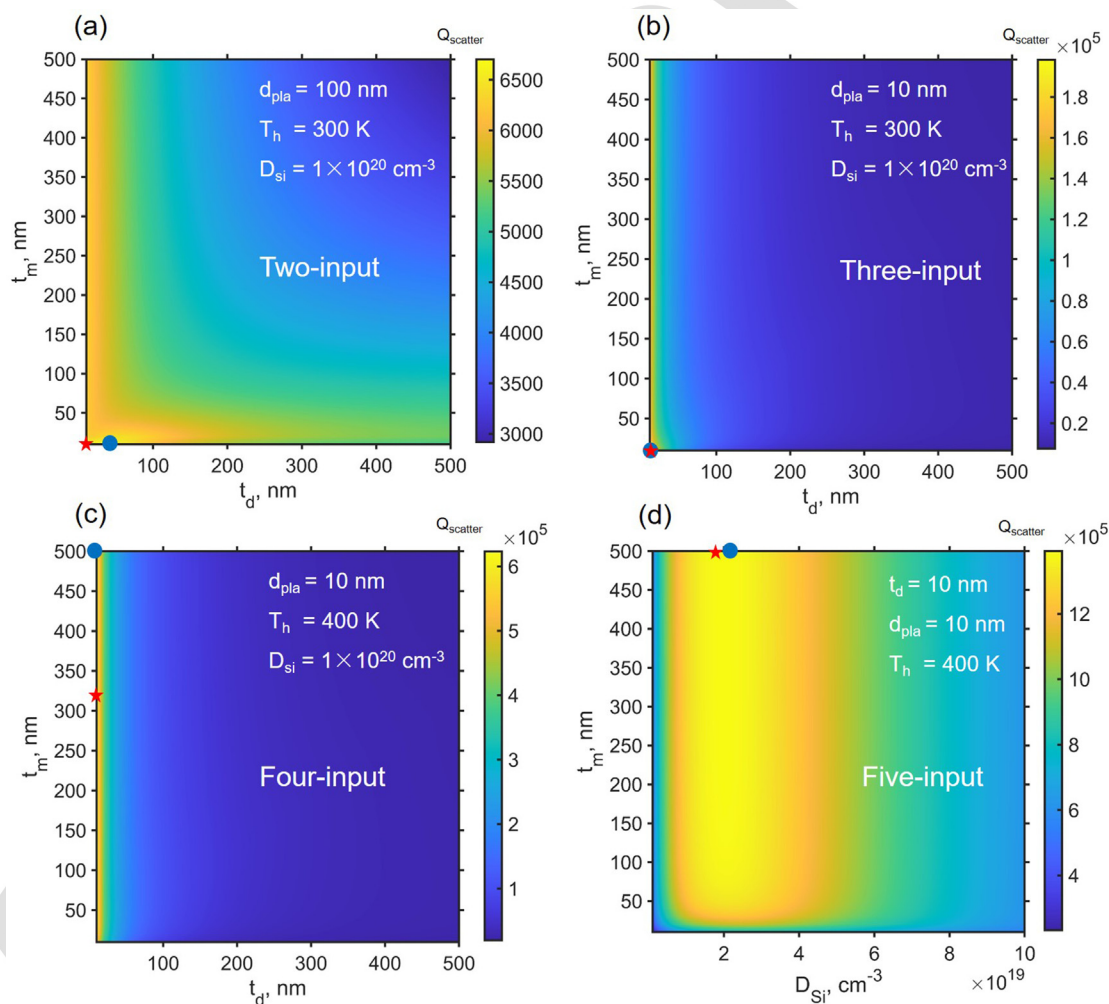


FIG. 4. NFRHT as a function of the thickness of D-Si t_m and Ge t_d in the (a) two-input model; (b) three-input model; (c) four-input model. (d) NFRHT as a function of the thickness of D-Si t_m and the doping concentration of D-Si D_{si} in the five-input model. The blue circle and red pentacle indicate the maximum NFRHT given by the rigorous scattering method and GA.

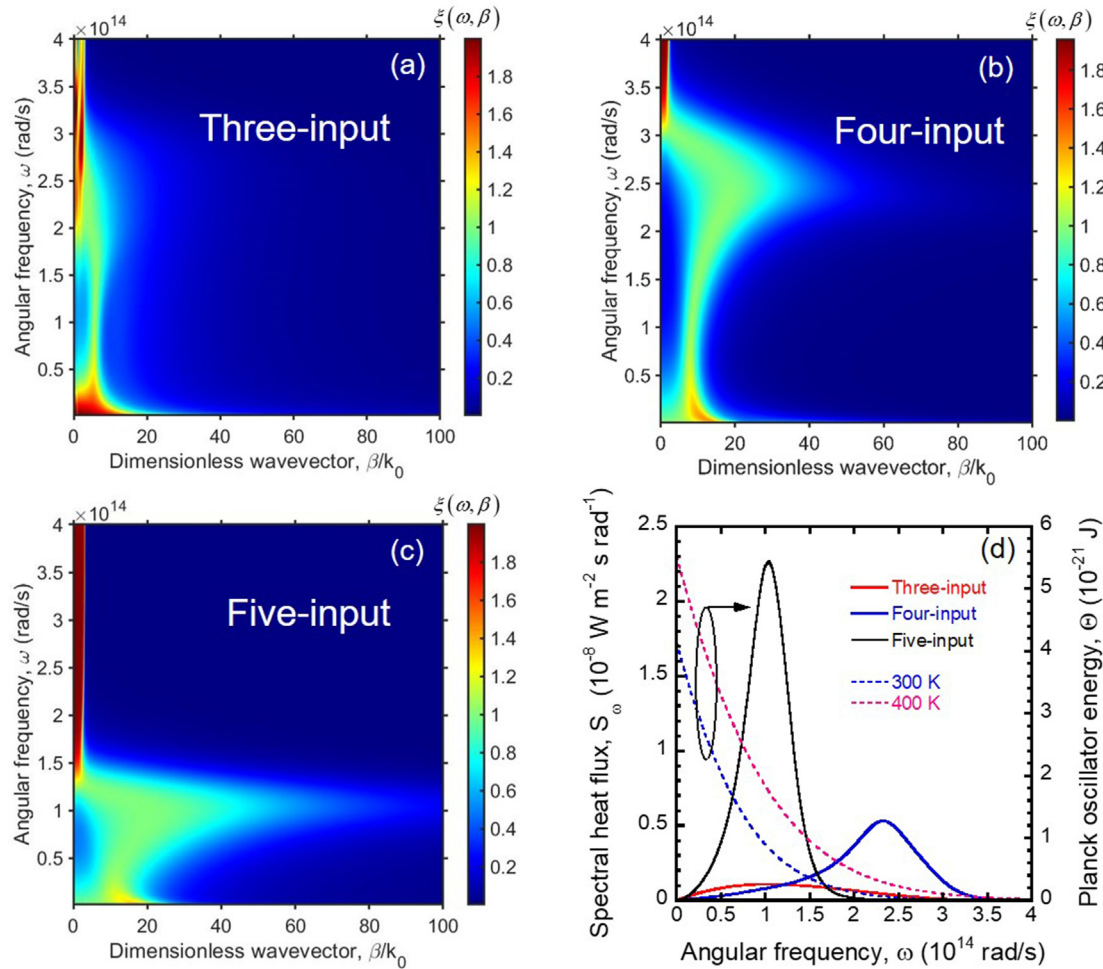


FIG. 5. Transmission coefficient contours $\xi(\omega, \beta)$ of the deterministic optimum for the (a) three-input model; (b) four-input model; (c) five-input model. Corresponding spectral heat flux and Planck oscillator energy are shown in (d).

values of input variables for the optimal output. Due to the high efficiency of inference for ANNs, the whole optimization process is taken no more than 1 min, and the corresponding results are shown in Table III. To verify the reasonability of results, we calculate the dependence of NFRHT as a function of design parameters using the rigorous scattering method and compare the optimal value with that given by GA. Physically speaking, we only need to look for the optimal t_m , t_d , and D_{Si} , because it is obvious to enhance the NFRHT by decreasing vacuum gap distances and improving the temperature difference between the emitter and receiver, so as to intensify the evanescent and propagating waves. For the two-input, three-input, and four-input model, NFRHT as a function of the thickness of D-Si t_m and Ge t_d are shown in Figs. 4(a)–4(c), respectively. For the five-input model, considering the optimal value for t_d in all models (two-input, three-input, four-input, and five-input) is 10 nm, and the NFRHT as a function of t_d and D_{Si} is only shown in Fig. 4(d). Optimal values obtained by scattering methods and GA are represented by blue circle and red pentacle, respectively. The results show that values determined by GA align well

with that determined by the rigorous scattering method in Figs. 4(a)–4(d). For the two-input and three-input model, the optimal region for NFRHT corresponds to the lower bound of t_m and t_d in Table I, which can be attributed to the well excitation of wideband hyperbolic modes.⁴⁵ For the four-input and five-input model, inversely, optimal values for t_m correspond to the upper bound in Table I. Although there exists a difference in Fig. 4(c), we find that the heat flux saturates and reaches nearly a constant when t_m is larger than 100 nm. This is because the whole system can be approximated as the NFRHT between two semi-infinite plates made of silicon with the gap distance equals to 20 nm, given that the dielectric function of Ge is constant. Therefore, the optimization results of the four-input and five-input model for $100 \leq t_m \leq 500$ are reasonable.

To elucidate the underlying mechanism for the change of optimal t_m value, contour plots are generated in Figs. 5(a) and 5(b) for three and four input cases to show the dependence of the transmission coefficient ξ (equals to $\xi_p + \xi_s$) on the lateral wave vector β and angular frequency ω . Figure 5(b) shows that ξ of the four-input model has

TABLE IV. Estimated time of the proposed workflow for the design of multilayered metamaterials.

Process	Accurate calculation	Model training	GA optimization
cost	3.4 h/1000 points	~10 min	~30 s

much larger contribution around 2.5×10^{14} rad/s mainly caused by the excitation of surface plasmon polaritons (SPPs) at the Si-vacuum interface, demonstrated by the SPP dispersion $k_{\text{SPP}} = \omega/c_0 \sqrt{\epsilon_{\text{D-Si}}/(1 + \epsilon_{\text{D-Si}})}$. At the same time, Fig. 5(d) shows that the Planck oscillator energy in high angular frequency will be activated at 400 K. Therefore, it will have a good match with the SPPs, and subsequently, a significant increase in spectral heat transfer in the high frequency band will occur, shown in Fig. 5(d). For the five-input model, we find that a lower dope concentration will lead to a higher value of the D-Si dielectric function's real part. This means that the ML algorithm can adjust its resonant frequency of the excited mode when the doping of silicon is further listed as the objective for optimization. The results show that GA accurately align its resonant frequency to region for high $\Theta(\omega, T)$ value, which gives rise to the larger enhancement of NFRHT, shown in Figs. 5(c) and 5(d). Above analysis verifies the correctness of deterministic optimum determined by the ANN and GA. It fully demonstrates the great potential of ML methods in the modeling and optimal design of NFRHT.

To illustrate the efficiency of our proposed ML method, the estimated time of each part in Fig. 1 for the design of multilayered metamaterials is listed in Table IV. In our workstation (Xeon E5-2697 v4), the consumed time for calculating 1000 points based on scattering methods is 3.4 h. Because we apply the second-order optimization algorithm, the rate of convergence for training the ANN model is very fast, and the consumed time is less than 10 min. After building the surrogate model, it only takes 30 s for GA to find the optimal design. In comparison, parametric analysis methods based on the rigorous

TABLE V. Range of considered variables for nanoparticles.

Parameter ^a	T_1	T_2	d_{par}	R_a	R_b
Lower bound	200	200	10	100	10
Upper bound	1000	1000	200	200	50

^aUnits for T_1 and T_2 are Kelvin (K). Units for d_{par} , R_a , and R_b are nanometer (nm).

scattering method are time consuming. For example, 2500 points are calculated to draw the 50×50 contour plot in Fig. 4 with only considering two variables. When considering five variables, conventional methods will take huge computational cost and are nearly impossible. We also need to mention that the training process is not fully optimized. There is still space to improve the speed and accuracy.

In order to verify the applicability of our proposed workflow in different structures and issues, another important categories in the near-field regime, viz., NFRHT and rectification ratio between nanoparticles, are further considered. In this paper, we consider the configuration of two nanospheres made of the same polytype of 3C-SiC.⁵⁰ The accurate NFRHT between two spheres can be derived by using dyadic Green's functions (DGFs) and the fluctuation-dissipation theorem, which is described in detail in Ref. 30. The performance of rectifiers can be characterized by the thermal rectification ratio as

$$R_{\text{ratio}} = \frac{Q_f - Q_r}{Q_r}, \quad (4)$$

where Q_f and Q_r are the net heat fluxes in the forward and reverse scenarios, respectively. As shown in Fig. 6, for the forward scenario, 3C-SiC with radius R_a is the emitter at the temperature of T_1 , and the receiver 3 C-SiC is maintained at T_2 . For the reverse scenario, temperatures of two spheres are switched, and the reverse NFRHT is Q_r . Gap distances for both scenarios are d_{par} .

Here, we only discuss the most complex condition, five-input model. The range of considered variables for sampling is shown in Table V.

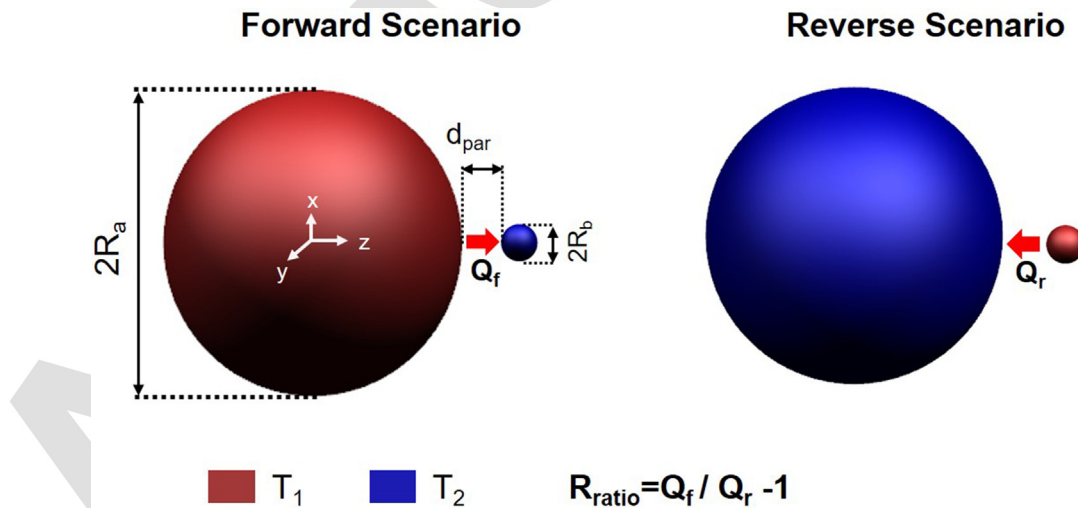


FIG. 6. Schematic diagram of NFRHT and thermal rectification between two nanospheres made of 3 C-SiC separated by a vacuum gap d_{par} . R_a and R_b represent the radius of sphere a and sphere b. T_1 and T_2 are set as the temperature of the emitter and receiver, respectively.

TABLE VI. Optimization results of trained ANN models for radiative heat flow and rectification ratio between nanoparticles.

Category ^a	T_1	T_2	d_{par}	R_a	R_b	Q_{ANN}	Q_{GF}	Error
Radiative heat flow	1000	506	10	200	50	27.96	27.81	0.5%
Rectification ratio	696	200	27.5	200	10	8.48	8.44	0.391%

^aUnits for Q_{ANN} , Q_{GF} are nW.

Training details of ANNs are in the [supplementary material](#). Deterministic parameters for the largest NFRHT and rectification ratio are shown in [Table VI](#). We can see that trained ANNs are accurate enough for predicting the value of deterministic optimum of nanoparticles and errors between predicted values, and accurate ones are no more than 1%. The deterministic parameters align well with results in [Ref. 50](#), which did more parametric analysis and calculations. This also demonstrates that the proposed workflow has great advantages in terms of the applicability in different issues and huge computational reduction.

To summary, by utilizing two mainstream ML algorithms, viz., ANN and GA, we reported a systematic workflow for modeling and optimal design of NFRHT. Through applying it to representative scenarios, including NFRHT between multilayer metamaterials, NFRHT, and thermal rectification between nanoparticles, we fully demonstrate its huge computational reduction and wide applicability in different NFRHT research works. These advantages are believed to have great potential in the future scientific research and industrial production. Next, better sampling methods and more advanced machine learning algorithms, such as convolutional/recurrent/graph neural networks in NFRHT, can be further explored. Spectral radiative heat transfer of arbitrary structures and materials is expected for modeling so as to better conduct the inverse design of the system.

See the [supplementary material](#) for detailed introduction of the ML strategy and training process of ANNs.

This work was mainly supported by the China National Key Research and Development Plan Project (Nos. 2018YFB1502000 and 2018YFA0702300) and the National Natural Science Foundation of China (Nos. 51706096 and 51820105010). X.L. also wants to thank the support by the Fundamental Research Funds for the Central Universities (No. 56XIA17001).

AUTHOR DECLARATIONS

Conflict of Interest

The authors have no conflicts to disclose.

Author Contributions

Shizheng Wen: Conceptualization (lead); Data curation (equal); Formal analysis (lead); Investigation (equal); Methodology (equal); Project administration (equal); Resources (equal); Software (equal); Validation (equal); Visualization (equal); Writing – original draft (lead); Writing – review and editing (equal). **Chunzhuo Dang:** Data curation (equal); Formal analysis (equal); Investigation (equal); Methodology (equal); Resources (equal); Software (equal); Validation

(equal); Visualization (equal); Writing – original draft (equal); Writing – review and editing (equal). **Xianglei Liu:** Conceptualization (equal); Funding acquisition (lead); Supervision (lead); Writing – review and editing (equal).

DATA AVAILABILITY

The data that support the findings of this study are available from the corresponding author upon reasonable request.

REFERENCES

¹X. Liu, L. Wang, and Z. M. Zhang, “Near-field thermal radiation: Recent progress and outlook,” *Nanoscale Microscale Thermophys. Eng.* **19**, 98–126 (2015).
²S.-A. Biehs, R. Messina, P. S. Venkataram, A. W. Rodriguez, J. C. Cuevas, and P. Ben-Abdallah, “Near-field radiative heat transfer in many-body systems,” *Rev. Mod. Phys.* **93**, 025009 (2021).
³W. Li and S. Fan, “Nanophotonic control of thermal radiation for energy applications,” *Opt. Express* **26**, 15995–16021 (2018).
⁴C. Lucchesi, R. Vaillon, and P.-O. Chapuis, “Radiative heat transfer at the nanoscale: Experimental trends and challenges,” *Nanoscale Horiz.* **6**, 201–208 (2021).
⁵E. Tervo, E. Bagherisereshki, and Z. Zhang, “Near-field radiative thermoelectric energy converters: A review,” *Front. Energy* **12**, 5–21 (2018).
⁶S. Molesky, P. S. Venkataram, W. Jin, and A. W. Rodriguez, “Fundamental limits to radiative heat transfer: Theory,” *Phys. Rev. B* **101**, 035408 (2020).
⁷C. Dang, X. Liu, H. Xia, S. Wen, and Q. Xu, “High-performance three-body near-field thermophotovoltaic energy conversion,” *J. Quant. Spectrosc. Radiative Transfer* **259**, 107411 (2021).
⁸R. Mittapally, B. Lee, L. Zhu, A. Reihani, J. W. Lim, D. Fan, S. R. Forrest, P. Reddy, and E. Meyhofer, “Near-field thermophotovoltaics for efficient heat to electricity conversion at high power density,” *Nat. Commun.* **12**, 4364 (2021).
⁹A. Fiorino, L. Zhu, D. Thompson, R. Mittapally, P. Reddy, and E. Meyhofer, “Nanogap near-field thermophotovoltaics,” *Nat. Nanotechnol.* **13**, 806–811 (2018).
¹⁰B. Zhao, P. Santhanam, K. Chen, S. Buddhiraju, and S. Fan, “Near-field thermophotonic systems for low-grade waste-heat recovery,” *Nano Lett.* **18**, 5224–5230 (2018).
¹¹S. Hassan, C. F. Doiron, and G. V. Naik, “Optimum selective emitters for efficient thermophotovoltaic conversion,” *Appl. Phys. Lett.* **116**, 023903 (2020).
¹²A. Kittel, W. Müller-Hirsch, J. Parisi, S.-A. Biehs, D. Reddig, and M. Holthaus, “Near-field heat transfer in a scanning thermal microscope,” *Phys. Rev. Lett.* **95**, 224301 (2005).
¹³A. Kittel, U. F. Wischnath, J. Welker, O. Huth, F. Rueting, and S.-A. Biehs, “Near-field thermal imaging of nanostructured surfaces,” *Appl. Phys. Lett.* **93**, 193109 (2008).
¹⁴Y. De Wilde, F. Formanek, R. Carminati, B. Gralak, P.-A. Lemoine, K. Joulain, J.-P. Mulet, Y. Chen, and J.-J. Greffet, “Thermal radiation scanning tunnelling microscopy,” *Nature* **444**, 740–743 (2006).
¹⁵M. Wong, C. Tso, T. Ho, and H. Lee, “A review of state of the art thermal diodes and their potential applications,” *Int. J. Heat Mass Transfer* **164**, 120607 (2021).
¹⁶S. Wen, X. Liu, S. Cheng, Z. Wang, S. Zhang, and C. Dang, “Ultrahigh thermal rectification based on near-field thermal radiation between dissimilar nanoparticles,” *J. Quant. Spectrosc. Radiative Transfer* **234**, 1–9 (2019).

- ¹⁷P. Ben-Abdallah and S.-A. Biehs, "Near-field thermal transistor," *Phys. Rev. Lett.* **112**, 044301 (2014).
- ¹⁸X. Liu, J. Shen, and Y. Xuan, "Pattern-free thermal modulator via thermal radiation between van der Waals materials," *J. Quant. Spectrosc. Radiative Transfer* **200**, 100–107 (2017).
- ¹⁹F. Chen, X. Liu, Y. Tian, Y. Liu, and Y. Zheng, "Self-adaptive near-field radiative thermal modulation using a thermally sensitive bimaterial structure," *Appl. Phys. Lett.* **119**, 221107 (2021).
- ²⁰W. Gu, G.-H. Tang, and W.-Q. Tao, "Thermal switch and thermal rectification enabled by near-field radiative heat transfer between three slabs," *Int. J. Heat Mass Transfer* **82**, 429–434 (2015).
- ²¹J. Shen, X. Liu, H. He, W. Wu, and B. Liu, "High-performance noncontact thermal diode via asymmetric nanostructures," *J. Quant. Spectrosc. Radiative Transfer* **211**, 1–8 (2018).
- ²²Y. Kan, C. Zhao, and Z. Zhang, "Near-field radiative heat transfer in three-body systems with periodic structures," *Phys. Rev. B* **99**, 035433 (2019).
- ²³K. Ito, K. Nishikawa, A. Miura, H. Toshiyoshi, and H. Iizuka, "Dynamic modulation of radiative heat transfer beyond the blackbody limit," *Nano Lett.* **17**, 4347–4353 (2017).
- ²⁴X. Wu and C. Fu, "Near-field radiative modulator based on dissimilar hyperbolic materials with in-plane anisotropy," *Int. J. Heat Mass Transfer* **168**, 120908 (2021).
- ²⁵X. Liu and Y. Xuan, "Near-field thermal radiation of metamaterials/metasurfaces constructed of natural anisotropic materials," *Annu. Rev. Heat Transfer* **23**, 95 (2020).
- ²⁶D. Xu, J. Zhao, and L. Liu, "Near-field thermal radiation of gradient refractive index slab: Internal polaritons," *Appl. Phys. Lett.* **119**, 141106 (2021).
- ²⁷J. Dai, F. Ding, S. I. Bozhevolnyi, and M. Yan, "Ultrabroadband superplanckian radiative heat transfer with artificial continuum cavity states in patterned hyperbolic metamaterials," *Phys. Rev. B* **95**, 245405 (2017).
- ²⁸Y. Kan and C. Zhao, "Near field radiative heat transfer in asymmetric three-grating systems," *Int. J. Heat Mass Transfer* **171**, 121124 (2021).
- ²⁹A. Narayanaswamy and Y. Zheng, "A Green's function formalism of energy and momentum transfer in fluctuational electrodynamics," *J. Quant. Spectrosc. Radiative Transfer* **132**, 12–21 (2014).
- ³⁰A. Narayanaswamy and G. Chen, "Thermal near-field radiative transfer between two spheres," *Phys. Rev. B* **77**, 075125 (2008).
- ³¹R. Li, Z. Liu, A. Rohskopf, K. Gordiz, A. Henry, E. Lee, and T. Luo, "A deep neural network interatomic potential for studying thermal conductivity of β -Ga₂O₃," *Appl. Phys. Lett.* **117**, 152102 (2020).
- ³²X. Wan, W. Feng, Y. Wang, H. Wang, X. Zhang, C. Deng, and N. Yang, "Materials discovery and properties prediction in thermal transport via materials informatics: A mini review," *Nano Lett.* **19**, 3387–3395 (2019).
- ³³T. Wang, C. Zhang, H. Snoussi, and G. Zhang, "Machine learning approaches for thermoelectric materials research," *Adv. Funct. Mater.* **30**, 1906041 (2020).
- ³⁴D. Visaria and A. Jain, "Machine-learning-assisted space-transformation accelerates discovery of high thermal conductivity alloys," *Appl. Phys. Lett.* **117**, 202107 (2020).
- ³⁵J. García-Esteban, J. Bravo-Abad, and J. C. Cuevas, "Deep learning for the modeling and inverse design of radiative heat transfer," *Phys. Rev. Appl.* **16**, 064006 (2021).
- ³⁶W. Zhang, B. Wang, and C. Zhao, "Selective thermophotovoltaic emitter with aperiodic multilayer structures designed by machine learning," *ACS Appl. Energy Mater.* **4**, 2004–2013 (2021).
- ³⁷P. Ben-Abdallah, K. Joulain, J. Drevillon, and G. Domingues, "Tailoring the local density of states of nonradiative field at the surface of nanolayered materials," *Appl. Phys. Lett.* **94**, 153117 (2009).
- ³⁸J. Drevillon and P. Ben-Abdallah, "Ab initio design of coherent thermal sources," *J. Appl. Phys.* **102**, 114305 (2007).
- ³⁹R. Hu, J. Song, Y. Liu, W. Xi, Y. Zhao, X. Yu, Q. Cheng, G. Tao, and X. Luo, "Machine learning-optimized Tamm emitter for high-performance thermophotovoltaic system with detailed balance analysis," *Nano Energy* **72**, 104687 (2020).
- ⁴⁰A. Sakurai, K. Yada, T. Simomura, S. Ju, M. Kashiwagi, H. Okada, T. Nagao, K. Tsuda, and J. Shiomi, "Ultrabroadband wavelength-selective thermal emission with aperiodic multilayered metamaterials designed by Bayesian optimization," *ACS Central Sci.* **5**, 319–326 (2019).
- ⁴¹J. Seo, P.-H. Jung, M. Kim, S. Yang, I. Lee, J. Lee, H. Lee, and B. J. Lee, "Design of a broadband solar thermal absorber using a deep neural network and experimental demonstration of its performance," *Sci. Rep.* **9**, 15028 (2019).
- ⁴²D. E. Rumelhart, J. L. McClelland, P. R. Group *et al.*, *Parallel Distributed Processing*, Vol. 1 (IEEE, New York, 1988).
- ⁴³K. Höschel and V. Lakshminarayanan, "Genetic algorithms for lens design: A review," *J. Opt.* **48**, 134–144 (2019).
- ⁴⁴M. A. Albadr, S. Tiun, M. Ayob, and F. Al-Dhief, "Genetic algorithm based on natural selection theory for optimization problems," *Symmetry* **12**, 1758 (2020).
- ⁴⁵X. Liu, T. Bright, and Z. Zhang, "Application conditions of effective medium theory in near-field radiative heat transfer between multilayered metamaterials," *J. Heat Transfer* **136**, 092703 (2014).
- ⁴⁶S. Basu, B. J. Lee, and Z. Zhang, "Infrared radiative properties of heavily doped silicon at room temperature," in *Proceedings of IMECE2007 2007 ASME International Mechanical Engineering Congress and Exposition*, Seattle, Washington, 11–15 November 2007.
- ⁴⁷M. T. Hagan, H. B. Demuth, and M. Beale, *Neural Network Design* (PWS Publishing Co., Boston, MA, 1997).
- ⁴⁸G. E. Karniadakis, I. G. Kevrekidis, L. Lu, P. Perdikaris, S. Wang, and L. Yang, "Physics-informed machine learning," *Nat. Rev. Phys.* **3**, 422–440 (2021).
- ⁴⁹Y. Cao, Z. Fang, Y. Wu, D.-X. Zhou, and Q. Gu, "Towards understanding the spectral bias of deep learning," in *30th International Joint Conference on Artificial Intelligence (IJCAI 2021)* (International Joint Conferences on Artificial Intelligence, 2021), pp. 2205–2211.
- ⁵⁰L. Zhu, C. R. Otey, and S. Fan, "Ultrahigh-contrast and large-bandwidth thermal rectification in near-field electromagnetic thermal transfer between nanoparticles," *Phys. Rev. B* **88**, 184301 (2013).